J Mater Sci (2025) 60:22615–22635

Chemical routes to materials

Synthesis and physicochemical characterization of a novel bismuth silicate templated by tetrapropylammonium bromide and polydiallyldimethylammonium chloride

Erick Paiva Cancella[1], Guilherme de Paula Guarnieri[1], Nader de Sousa Amadeu[2], Martin Radtke[2], Rodrigo Henrique Garcia[3], Eduardo Ribeiro de Azevedo[3], Ivana Conte Cosentino[4], Yvonne Primerano Mascarenhas[3], and José Geraldo Nery[1,*]

[1] *Department of Physics, São Paulo State University (UNESP), Campus of Sao José Do Rio Preto, Sao José Do Rio Preto, SP 15054-000, Brazil*
[2] *Division 1.3 Structure Analysis, NMR Spectroscopy, BAM Federal Institute for Materials Research and Testing, Richard Willstaetter Str. 11, 12489 Berlin, Germany*
[3] *São Carlos Institute of Physics, University of São Paulo, São Carlos, SP 13566-590, Brazil*
[4] *Nuclear and Energy Research Institute (IPEN), Av. Prof. Lineu Prestes 2242, Sao Paulo, SP 05508-000, Brazil*

Received: 8 February 2025
Accepted: 21 October 2025
Published online:
3 November 2025

ABSTRACT

A bismuth silicate (BiSi-1) was hydrothermally synthesized using tetrapropylammonium bromide (TPA·Br) as the organic structure-directing agent and shown by multi-scale characterization to be distinct from known Bi–silicates. Powder X-ray diffraction is indexable with an orthorhombic metric (a = 23.234 Å, b = 17.109 Å, c = 3.897 Å), consistent with a highly anisotropic, possibly layered framework. High-resolution TEM/SAED reveals nanocrystalline, plate-like domains assembled into sub-micrometric aggregates with locally oriented lamellae; lattice fringes (0.27–0.32 nm) match the strongest XRD spacings. Solid-state NMR establishes a silica-rich network with a dominant Q^4 population (77%) and minor Q^3 (11%) and Q^2 (12%) sites; the contact-time dependence of ^1H to ^{29}Si cross-polarization is consistent with increasing proximal-proton density from Q^4 to Q^2. Aging to 24 h sharpens the ^{29}Si lineshape, while calcination progressively removes the OSDA and vicinal hydroxyls; at 750 °C, ^{29}Si spectra indicate framework densification/rearrangement. XANES/EXAFS places bismuth predominantly as Bi^{3+} in an oxide-like environment with a pronounced Bi–O first shell and no detectable Bi^0 or Bi–Br contributions. ICP–OES yields a reproducible Bi/Si atomic ratio of 1:3. Thermogravimetry shows stepwise desorption, dehydroxylation, and template removal, with thermal stability maintained to 750 °C. Nitrogen sorption confirms mesoporosity in the as-made and Soxhlet-extracted solids (the latter exhibiting

Handling Editor: Julia Glaum.

Address correspondence to E-mail: geraldo.nery@unesp.br

https://doi.org/10.1007/s10853-025-11732-6

the highest surface area), whereas high-temperature calcination reduces porosity. Collectively, BiSi-1 emerges as a nanocrystalline, anisotropic Bi–silicate whose connectivity, local Bi–O environment, and accessible texture are tunable by aging and post-treatments, positioning it as a promising platform for heterogeneous catalysis and environmental remediation.

Introduction

Zeolites are microporous crystalline solids composed of silicon, aluminum, and oxygen frameworks, often accompanied by extra-framework species such as water and exchangeable cations. These materials exhibit exceptional physicochemical properties, including high thermal stability, strong acidity, ion-exchange capacity, large specific surface area, and a well-defined microporous structure that enables shape-selective catalysis and molecular sieving. The substitution of Si^{4+} by Al^{3+} in the zeolitic framework introduces negative charges that are balanced by cations residing within the pores. Beyond classical aluminosilicates, molecular sieves can incorporate other heteroatoms—such as Ti^{4+}, Ge^{4+}, Ga^{3+}, and Zn^{2+}—leading to a broader class of porous materials with tailored functionalities [1, 2].

Of particular interest are metallosilicates with mixed octahedral–pentahedral–tetrahedral (OPT) coordination geometries, where transition metals or lanthanides are integrated into the crystalline framework. These OPT materials have gained attention due to their enhanced redox properties and potential catalytic applications [3–5]. Although several families of microporous OPT materials have been developed—such as vanadosilicates, titanosilicates, zirconosilicates, niobiosilicates, stannosilicates, and lanthanide silicates [3–5]—bismuth-containing analogs remain underexplored.

Bismuth compounds display unusual structural diversity owing to the large ionic radius and stereochemically active $6s^2$ lone pair of Bi^{3+}. In solution, Bi^{3+} salts undergo extensive hydrolysis, readily forming oxyspecies and polynuclear aggregates with flexible coordination geometries. This structural plasticity underpins applications ranging from metallurgical alloys and additives to thermo-/ferroelectrics, pigments, and heterogeneous catalysts. Over the past decades, Bi-based materials spanning distinct crystallographic types and micro-/nanoscale morphologies have been obtained by multiple routes, including (i) aqueous hydrolysis at ambient temperature, (ii) hydrothermal/solvothermal synthesis, (iii) high-temperature annealing/calcination, and (iv) thin-film or particulate methods such as cathodic sputtering and pulsed-laser deposition. These techniques enable 3D hierarchical architectures—nanosheets, nanotubes, nanospheres, nanowires, and related assemblies—with tailored physicochemical properties [6, 7].

In homogeneous catalysis, organobismuth compounds have been widely used in synthetic transformations [8, 9]. In the field of heterogeneous catalysis, Bismuth has been incorporated into a wide range of micro- and mesoporous supports—zeolitic MFI (ZSM-5) [10–13], BEA [14, 15], FAU (Y) [16–19], FER [20], GIS/zeolite-P [21] and mesoporous silicas MCM-41 [22–25], SBA-15 [26–31], and TUD-1 [32–34]—yielding catalysts that couple the shape-selective confinement and Brønsted/Lewis acidity of the host with the redox/Lewis acidity of Bi species (Bi^{3+}/Bi^{5+}; Bi_2O_3/BiO_x clusters). This synergy enables both acid–redox co-catalysis and selective oxidations, exemplified by Bi-modified MFI in liquid-phase oxidations and base synthesis [10, 11], high-pressure Bi insertion into silicalite-1 (S-1) that expands structural/optical functionality [13], and Bi-MCM-41/SBA-15/TUD-1 systems active in cyclohexane oxidation, photocatalysis, and low-temperature CO oxidation [23, 25, 26, 29, 32–34]. In biomass valorization, Bi-decorated Beta (BEA) exhibits high selectivity for aerobic cellulose conversion to glycolic acid [15]. In environmental catalysis, Bi implanted on FER drives efficient NO_x reduction by methanol (MeOH-SCR) [20], while Bi embedded or reduced on SBA-15 and Bi-modified BEA afford strong radioiodine capture via Bi–I adduct formation and stable immobilization [14, 27, 30, 31]. Beyond catalysis and separations, low-valent Bi centers confined in FAU (Y) and MFI/MOR channels display ultra-broadband near-IR photoluminescence relevant to sensing/optical applications [12, 16–18]; related Bi-zeolite composites can also host plasmonic/photocatalytic nanoparticles, enabling size-dependent photoactivity [19]. Practically, performance can be tuned by framework choice (MFI/BEA/FER/FAU/GIS vs. MCM-41/SBA-15/TUD-1), Si/Al ratio, Bi loading/speciation (ion exchange, impregnation, solid-state routes), and post-treatments (calcination/

reduction) that control dispersion and oxygen-vacancy chemistry; conversely, stability demands attention to Bi_2O_3 phase changes, sintering/migration under steam, and poisoning by sulfur/halides, which can be mitigated by strong anchoring to framework oxygens and defect engineering. Taken together, Bi–zeolite hybrids offer a versatile platform spanning selective catalysis, pollutant capture/remediation, and optically active materials [10–34].

By contrast, microporous bismuth silicates with zeolite-like open frameworks remain exceptionally rare [35, 36]. To the best of our knowledge, only EMS-4 and EMS-5 have been reported—both synthesized hydrothermally by Zanardi et al. [37] using tetramethylammonium hydroxide (TMAOH) as the organic structure-directing agent (OSDA). EMS-4 exhibits a layered arrangement with wide channels capable of accommodating extra-framework cations and water, whereas EMS-5 features a clathrate-like framework composed of small cages. Notably, although TMAOH was employed during the synthesis of EMS-5, no organic or water molecules were localized within the cages after crystallization, as confirmed by crystallographic refinement, thermogravimetry, and IR spectroscopy—underscoring the role of OSDAs in templating framework assembly even when they are not retained in the final solid [37].

Against this backdrop, the incorporation of bismuth into crystalline, zeolite-type silicate frameworks using alternative OSDAs remains virtually unexplored. Here, we report the hydrothermal synthesis and physicochemical characterization of a new microporous bismuth silicate prepared with two distinct organic templates—tetrapropylammonium bromide (TPA·Br) and polydiallyldimethylammonium chloride (PDADMAC)—an OSDA pair not previously documented for bismuth silicate synthesis. We systematically vary the sol–gel aging conditions to modulate nucleation, phase selectivity, and pore development, and we show that the resulting material exhibits framework features and surface properties that make it a promising candidate for heterogeneous catalysis and environmental remediation.

Experimental section

Hydrothermal synthesis of bismuth silicates

A typical synthesis described here used Ludox HS-30 (SiO_2, 30% by weight, Sigma-Aldrich) as the sole source of silica, sodium hydroxide (NaOH, 97%, Sigma-Aldrich) as the basic agent, and $Bi(NO_3)_3{\cdot}5H_2O$ (Sigma-Aldrich) as the bismuth source. The structure-directing agents (SDA) used were either tetrapropylammonium bromide (TPA.Br, $(CH_3CH_2CH_2)_4N(Br)$, 98%, Sigma-Aldrich) or polydiallyldimethylammonium chloride (PDADMAC, $(C_8H_{16}NCl)_n$, Sigma-Aldrich, 20% by weight in H_2O). Three different batches prepared, according to the SDA: one with TPA.Br, another with PDADMAC, and a third batch without any SDA. For the two first cases, the molar ratio between Si and the SDA was always kept constant at 0.2. Ludox and NaOH were added to the reaction mixture, following the molar ratio of 5.19 SDA: Bi_2O_3: 24 Na_2O: 5.25 SiO_2: 387 H_2O, and the mixture was kept under magnetic stirring (850 rpm) for 1 h. The pH was then measured, and the solution was left at rest. Subsequent pH measurements were performed at 6, 12, 24, 48, and 72 h after stirring had stopped. The resulting gel was transferred to a reactor (model 4748, Parr) and heated in an oven (model 315 SE, FANEM, Brazil) at 200 °C, under autogenous pressure, for 7 days. Finally, the solid was obtained and the mother liquor was stored at room temperature. The solid was filtered under vacuum, at room temperature, washed three times with deionized water and acetone (ACS reagent), and was then dried overnight at 90 °C in an oven. For further analysis, the material aged 24 h, and 12 h was designated as Bismuth Silicate-1 (BiSi-1) and Bismuth Silicate-2 (BiSi-2), respectively.

For removal of the organic templates, two different processes were applied, namely calcination and Soxhlet extraction. Calcination of the BiSi-1 sample was performed by heating the material in a muffle furnace, using a heating rate of 10 °C min^{-1} up to target temperatures of 450 °C (BiSi-3), 550 °C (BiSi-4), or 750 °C (BiSi-5), maintaining the final temperature for 8 h before cooling to room temperature. Soxhlet extraction was performed using an ethanol:dichloromethane mixture (1:9 ratio), at 90 °C, under stirring, and reflux was named BiSi-6.

Physicochemical characterization

X-ray diffraction

X-ray diffractograms of the synthesized films were acquired using a MiniFlex II diffractometer (Rigaku, Tokyo, Japan) equipped with a graphite monochromator and a rotary anode source consisting of a flat plate, in Bragg–Brentano geometry. The instrument operated with Cu Kα radiation (wavelength = 1.5418 Å), at 40 kV and 15 mA. The diffractograms were recorded in the 2θ range 3–50°, at a scan speed of 2° (2θ) min^{-1}.

Infrared spectroscopy (FT-IR)

FT-IR spectra were obtained using a Shimadzu IRTracer-100 spectrometer, in the range from 400 to 4000 cm^{-1}, with resolution of 4 cm^{-1}, step size of 1 cm^{-1}, and averaging of 64 scans. The samples were prepared in the form of KBr pellets containing about 10% by weight of the test material.

Inductively coupled plasma-optical emission spectroscopy (ICP-OES)

Quantitative elemental chemical analysis of Si, Na, and Bi in the compositions of the materials was performed by optical emission spectroscopy, at the Analytical Center of the University of São Paulo (USP-SP), using a SPECTRO ARCOS radial ICP-OES instrument. The samples were digested using a mixture of hydrofluoric acid and 4% boric acid solution (1:12 ratio), with heating at 100 °C in sealed flasks on a digestion block.

Scanning electron microscopy (SEM) and transmission electron microscopy (TEM)

Scanning electron microscopy (SEM) images were recorded using FEI Magellan 400 L and Philips XL-30 FEG instruments, both coupled to energy-dispersive X-ray (EDS) analyzers and operated with adjustable electron beam voltages from 5 to 25 kV. Prior to the analyses, a thin coating of gold was deposited on the samples. TEM images were acquired with an FEI Tecnai G2 F20 instrument. HRTEM images and corresponding EDX maps were obtained using an FEI Tecnai G2 F20 instrument equipped with an energy-dispersive X-ray spectrometer (EDX) with a super ultra-thin window (SUTW). The experiments were carried out at the Structural Characterization Laboratory of the Federal University of São Carlos (LCE/DEMa/UFSCar).

Thermogravimetric analyses (TGA)

Thermogravimetric analyses of the materials were performed at the Analytical Center of the Institute of Chemistry (University of São Paulo, São Paulo), using a TGA Q500 analyzer (V20.13, Build 39, TA Instruments, New Castle). The samples were heated from 25 to 900 °C, at 10 °C min^{-1}, in an N_2 atmosphere (40 mL min^{-1}), followed by an isothermal step (900 °C) for 60 min in a synthetic air atmosphere (60 mL min^{-1}). The equipment was calibrated using a $CaC_2O_4.H_2O$ analytical standard (Sigma-Aldrich). For the analysis, 15 mg of the sample was placed in a platinum (Pt) crucible.

Textural characterization

Nitrogen adsorption isotherms were acquired at the temperature of liquid nitrogen, -196.15 °C (~ 77 K), using a Micromeritics ASAP 2020 analyzer. The sample was degassed under vacuum at 200 °C for 12–16 h prior to the measurement, to remove physically bonded surface impurities, including moisture. Due to the microporosity of the materials, after transfer to the analysis port, a second degassing step with heating was applied, to ensure that the micropores were free of moisture or contamination with other vapors. The specific surface areas of the bismuth silicates were calculated using the standard Brunauer–Emmett–Teller (BET) method [38]. The Barrett–Joyner–Halenda (BJH) model was used to derive the pore volumes and pore size distributions from the adsorption branches of the isotherms. The total pore volume, VPt (cm^3 g^{-1}), was estimated from the amount adsorbed at the maximum relative pressure (P/P_0 of 0.995), using the BJH method, together with the pore distribution (PSD) and the average pore size [39], employing the relation between capillary condensation pressure and pore diameter established by Kruk et al.. The micropore volume, Vmi (cm^3 g^{-1}), was determined by the Horvath–Kawazoe (HK) method, which is a semi-empirical adsorption model employed to calculate the micropore size distribution [40].

XANES and EXAFS analysis

X-ray absorption near edge structure (XANES) and extended X-ray absorption fine structure (EXAFS) measurements were performed at the BAMline of the BESSY II synchrotron radiation facility, Helmholtz-Zentrum Berlin, Germany [40]. The Bi L3-edge (13.418 keV) was selected for XANES measurements. However, due to the proximity of the Br K-edge

(13.474 keV) present in the samples, EXAFS measurements at the Bi L3-edge were not feasible. Instead, the Bi L1-edge (16.385 keV) was used for EXAFS analysis.

The samples consisted of finely ground powders, mounted between Kapton® tape layers and measured in transmission mode. Ionization chambers were employed for incident and transmitted beam detection. An Si(111) double-crystal monochromator (DCM) provided high energy resolution ($\Delta E/E = 1.37 \times 10^{-4}$). No detuning was applied. The beam size at the sample was approximately 1.0 mm (H) × 0.5 mm (V).

Energy scans were collected continuously, triggered at equidistant steps of the monochromator angle, resulting in an effective step size of ~ 0.5 eV. The scanned range extended from ~ 100 eV below to ~ 900 eV above the respective absorption edge. For EXAFS evaluation, energy regions affected by monochromator glitches or spectral artifacts were excluded. Each spectrum contained ~ 2000 data points. For each sample, three consecutive scans (each ~ 2 min duration) were recorded and averaged to improve the signal-to-noise ratio.

Energy calibration was performed using a 5 µm thick Bi foil reference. Samples (EC-1 and EC-2) were positioned on a three-axis motorized stage for precise alignment. All measurements were carried out at room temperature. Three different positions were probed on each sample, with no significant spectral variations observed between repeated measurements [41, 42].

Data reduction and normalization were carried out using the ATHENA software package [43]. A comprehensive description of the BAMline instrumentation and optical components is available elsewhere [42].

Magic-angle spinning (MAS) solid-state (SS) NMR

Magic-angle spinning (MAS) solid-state (SS) NMR spectra of ^{29}Si [44] were obtained at the São Carlos Institute of Physics, University of São Paulo, using a Bruker Avance spectrometer operating with a static field of 9.4 T. The instrument was equipped with a 7-mm double resonance Jackobsen design probe head, with a pneumatic sample rotation system, providing frequency stability greater than 2 Hz. Single-pulse excitation experiments under MAS (^{29}Si SPEMAS) were performed at 6 kHz MAS frequency, using a recycle delay of 20 s to achieve more quantitative ^{29}Si spectra. Experiments with ^{1}H-^{29}Si cross-polarization (^{1}H-^{29}Si CPMAS) were performed with a power ramp (80–100%) in the ^{1}H radiofrequency channel, MAS frequency of 6 kHz, and 5 s recycle delay. In both CPMAS and SPEMAS experiments, ^{1}H decoupling was achieved using a SPINAL-64 decoupling pulse sequence, with a field of 60 kHz, during an acquisition time of 15 ms. Zirconia rotors were used in all the experiments, with the absence of background signals confirmed by measuring empty rotors. The ^{29}Si chemical shifts were calibrated using kaolinite as an external reference.

Further ^{13}C CP MAS NMR experiments were performed at the German Federal Institute for Materials Research and Testing (BAM) in Berlin, using a Bruker Avance spectrometer, with a static field of 14 T. For the ^{13}C measurements, the sample was packed into a 2.5-mm zirconia rotor and spun at 25 kHz along the magic angle (MAS), in a double-resonant wide-bore probe, at room temperature. Cross-polarization was applied with contact times of 9 ms, and the ^{1}H-channel power was ramped. During a typical acquisition time of about 10 ms, ^{1}H was decoupled using the spinal64 sequence. Very long experiments with accumulations of between 16 and 64 k scans were performed to overcome the low sensitivity observed for the samples. Using the same hardware described above, ^{1}H measurements were performed with application of the EASY pulse program proposed by Jaeger and Hermann [45] for background signal removal. Two 90° pulses were applied, with a slight delay between them. By subtracting the FID after each of these pulses, the background signal was effectively eliminated. For ^{29}Si measurements, the samples were packed into 4-mm zirconia rotors and spun at 15 kHz along the magic angle (MAS), in a double-resonant wide-bore probe, at room temperature. Cross-polarization was applied, with parameters similar to those for ^{13}C nuclei. Again, longer accumulations were required to achieve the desired signal-to-noise ratio.

Results and discussion

X-ray diffraction (XRD)

The chemical composition of BiSi-1 was quantified by ICP–OES using two independent digestions to assess reproducibility. Elemental contents were Bi 39.60/39.18 wt%, Si 13.13/13.15 wt% and Na 4.76/4.79 wt% (means ± SD: Bi 39.39 ± 0.30 wt%, Si 13.14 ± 0.01 wt%, Na 4.775 ± 0.021 wt%; RSD ≤ 0.8%).

Conversion to atomic proportions yields a Bi:Si ratio of ~ 1:(2.48 ± 0.02), confirming bismuth incorporation in the silicate matrix.

The effect of sol–gel aging on formation of the structure bismuth silicate using TPA.Br as organic template were fully studied varying from no sol–gel aging until 72 h aging. Samples obtained varying the sol–gel aging time from 0 to 12 h showed crystalline phases identified as cristobalite (JCPDS 030267), bismite (JCPDS 27–0053) and δ-Bi_2O_3 phase (JCPDS No. 52–1007) and from 48 to 72 h several competitive phases were identified such as Bismite (JCPDS 27–0053); β-Bi_2O_3 (JCPDS 78–1793); cristobalite (JCPDS 030267); quartz (JCPDS 47–1144); δ-Bi_2O_3 (JCPDS No. 52–1007) (Figure SF1, Supplementary Material). A distinct and well-defined crystalline phase was only obtained with aging 24 h resulting in a structure with well-defined Bragg diffraction reflections at $2\theta = 3.79°$, 6.36°, 7.72°, 24.66°, 27.95°, 28.59°, 31.09°, 32.24°, and 33.03° and further analysis and discussion were performed with this sample (Fig. 1).

Wei et al. [46] obtained Bi_2SiO_5 from silica-aerogel precursors in two well-known polymorphs—an orthorhombic phase (JCPDS 36–0287; a = 15.217 Å, b = 5.477 Å, c = 5.325 Å; $Cmc2_1$) and a tetragonal phase (JCPDS 36–0288; a = b = 3.802 Å, c = 15.194 Å)—whereas the phase isolated here after 24 h aging (BiSi-1) exhibits a distinct diffraction signature with sharp Bragg reflections at $2\theta = 3.79°$, 6.36°, 7.72°, 24.66°, 27.95°, 28.59°, 31.09°, 32.24°, and 33.03° (Cu Kα), which was indexed by TREOR [47] to an orthorhombic metric a = 23.234 Å, b = 17.109 Å, c = 3.897 Å ($\alpha = \beta = \gamma = 90°$) (Table ST1 See Supplementary Material). These lattice parameters are not commensurate with either of Wei's cells by simple super/subcell relations: BiSi-1 has markedly enlarged in-plane repeats (a and b) and a much shorter out-of-plane repeat (c), immediately excluding assignment to the reported orthorhombic or tetragonal Bi_2SiO_5. The intense very-low-angle reflection at 3.79° ($d \approx 23.3$ Å), together with additional low-angle lines at 6.36° ($d \approx 13.9$ Å) and 7.72° ($d \approx 11.4$ Å), indicates large real-space periodicities parallel to the basal plane and a short repeat along c, a combination that is characteristic of strong metric anisotropy and consistent with a layered or sheet-like architecture. This behavior aligns with the broader chemical propensity of Bi^{3+} oxo-compounds—governed by the large ionic radius and stereochemically active $6s^2$ lone pair—to assemble anisotropic frameworks, yet it departs decisively from the denser Bi_2SiO_5 polymorphs accessed from aerogels. In practical terms, our synthesis/aging protocol accesses a crystallographically different bismuth silicate archetype, likely stabilized by an alternative assembly pathway (e.g., OSDA-assisted or defect-templated ordering) that generates expanded in-plane periodicities not present in the known Bi_2SiO_5 cells. Ongoing Le Bail/Rietveld tests of alternative space groups, together with SAED and

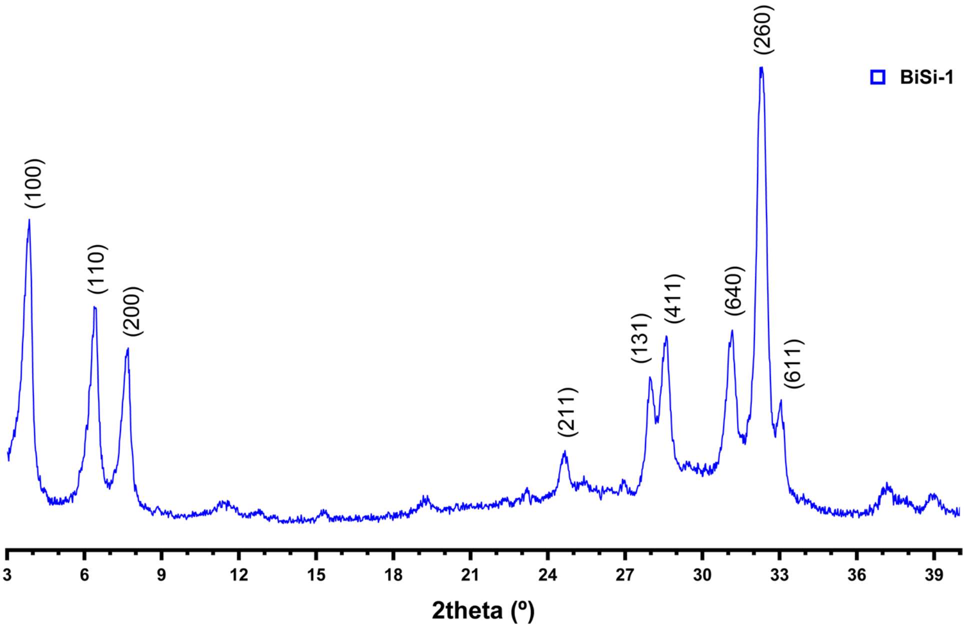

Figure 1 Powder X-ray diffraction (XRD) pattern of bismuth silicate BiSi-1 synthesized hydrothermally using tetrapropylammonium bromide (TPA·Br) as the organic structure-directing agent after 24 h sol–gel aging.

HRTEM along [001], will refine the symmetry assignment and probe whether the low-angle order arises from framework porosity and in-plane modulation or from layer stacking with registry. Taken together, the cell metrics and diffraction pattern demonstrate that BiSi-1 is a crystallographically distinct, strongly anisotropic (layer-like) bismuth silicate, extending the structural landscape beyond the Bi_2SiO_5 polymorphs of Wei et al. and indicating a new route to open, layered Bi–silicate frameworks.

Since the seminal work of Breck [48] and subsequent analyses by Zhdanov [49] and Mintova [50], crystalline zeolites are recognized as metastable products whose outcome is exquisitely sensitive to raw-material reactivity, reagent addition order, agitation, and—crucially—gel aging. Aging typically shortens the induction period and accelerates crystallization; in many aluminosilicates, it can also shift phase selectivity. For bismuth silicates, however, systematic studies of aging effects are scarce. In our syntheses, impurity phases reported by Zanardi et al. [37] (e.g., eulytite, $Bi_4Si_3O_{12}$) were not observed. Instead, we find that alkalinity and sodium content exert a pivotal influence on phase formation: the only condition that yielded a well-defined crystalline phase (BiSi-1)—indexed to an orthorhombic metric $a = 23.234$ Å, $b = 17.109$ Å, $c = 3.897$ Å ($\alpha = \beta = \gamma = 90°$)—was a batch with pH = 10.4 and the molar composition *5.19 OSDA: 1* Bi_2O_3*: 24* Na_2O*: 5.25* SiO_2*: 387* H_2O (OSDA = TPA·Br), aged 24 h prior to hydrothermal treatment. Under these same conditions, the mother liquor left at room temperature spontaneously yielded $NaNO_3$ single crystals after ~ 15 days; single-crystal XRD (XtaLAB Synergy-S) gave a = b = 5.0688(4) Å, c = 16.5247(18) Å in the hexagonal setting, confirming sodium nitrate. By contrast, syntheses prepared with other aging times did not produce crystalline Bi–silicate, and no $NaNO_3$ crystallized from their mother liquors even after three months at ambient conditions. Likewise, replacing TPA·Br with the polycationic OSDA PDADMAC failed to produce a crystalline Bi–silicate for any aging time (Fig. 2), indicating that the OSDA choice alone is insufficient to direct Bi–silicate crystallization in the absence of the appropriate alkali regime.

This co-occurrence—BiSi-1 formation together with exsolved $NaNO_3$ from the same liquid phase—does not, by itself, prove causation; however, it is a robust indicator of the solution speciation window in which Bi–silicate nucleation succeeds. Given that the Bi precursor is $Bi(NO_3)_3$, the appearance of bulk $NaNO_3$ implies that, at pH ≈ 10.4 and elevated $[Na^+]$, nitrate becomes sufficiently supersaturated to crystallize from the mother liquor, while Bi^{3+} is largely partitioned into oxo/hydroxo-silicate oligomers. In this regime, Na^+

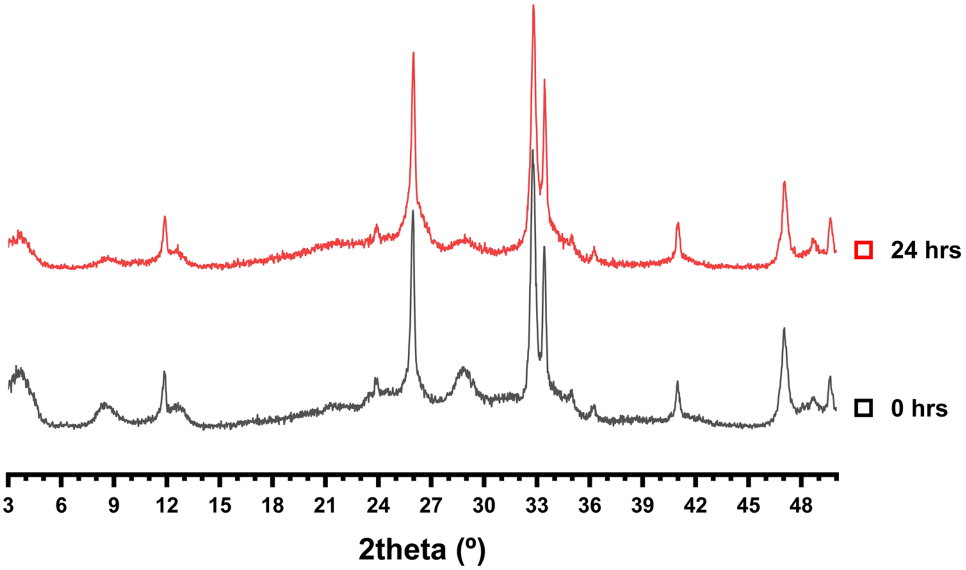

Figure 2 Powder X-ray diffraction (XRD) patterns of bismuth silicates synthesized with polydiallyldimethylammonium chloride (PDADMAC) as the polymeric structure-directing agent under the same hydrothermal conditions used for BiSi-1 (TPA·Br), at varying sol–gel aging times. While faint Bragg features are present, the diffractograms do not reproduce the phase-pure BiSi-1 obtained with TPA·Br; instead, they show broad backgrounds and/or non-matching reflections, consistent with low crystallinity and/or mixed-phase products.

plausibly promotes (i) silica deprotonation and growth of anionic silicate species, (ii) charge compensation and stabilization of Bi–oxo–silicate clusters, and (iii) a pre-nucleation equilibrium favorable to the layer-like, strongly anisotropic framework ultimately observed for BiSi-1 ($a,b \gg c$). Conversely, when this alkali/speciation window is not reached—either by altering the aging time or by substituting the OSDA—the system stalls in poorly ordered Bi–oxo–silicate precipitates, and no $NaNO_3$ crystallizes, signaling a different ionic balance in the mother liquor.

Taken together, these results emphasize that in Bi–silicate syntheses the inorganic cation population (here, Na^+), not just the OSDA identity and aging protocol, is a determinant of phase selectivity. The correlation between BiSi-1 crystallization and $NaNO_3$ exsolution marks a narrow chemical window where alkalinity, nitrate balance, and OSDA action align to enable nucleation of the orthorhombic, highly anisotropic Bi–silicate. This provides a practical handle for rationally tuning gel chemistry in future work—e.g., through controlled [Na^+], counter-anion management, and aging-time mapping—to expand access to crystalline Bi–silicate frameworks.

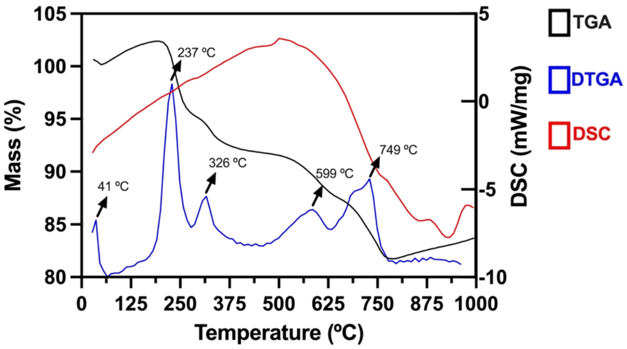

Figure 3 Thermogravimetric (TGA) and derivative thermogravimetric (DTG) profiles of bismuth silicate BiSi-1. Five mass-loss events are resolved: (i) ~ 1.05% at ≈ 41 °C from desorption of physisorbed water; (ii) 7.71% at ≈ 237 °C, consistent with dehydroxylation of bismuth hydroxide formed by precursor hydrolysis, $Bi(OH)_3 \rightarrow BiO(OH) + H_2O$; (iii) 2.95% at ≈ 326 °C from further dehydration to bismuth(III) oxide, $2\ BiO(OH) \rightarrow Bi_2O_3 + H_2O$; (iv) 3.47% at ≈ 599 °C attributed to oxidative decomposition/combustion of occluded tetrapropylammonium (TPA^+) residues; and (v) 7.58% at ≈ 749 °C assigned to framework densification/partial collapse driven by condensation of surface/defect silanols [51–53].

Thermogravimetric analysis (TGA)

Thermogravimetric (TGA) and derivative thermogravimetric (DTG) analyses were used to monitor the removal of physisorbed water and the structure-directing agent (SDA) from the material (Fig. 3). Five discrete mass-loss events were resolved. An initial 1.05% loss at 41 °C is assigned to desorption of externally adsorbed water. A second event at ≈ 237 °C (7.71%) is consistent with thermal dehydroxylation of bismuth hydroxide formed by precursor hydrolysis: $Bi(OH)_3 \rightarrow BiO(OH) + H_2O$. In agreement with the XRD evidence for an intermediate rearrangement, this step plausibly yields bismuth (III) oxyhydroxide (BiO(OH), often written BiOOH), a well-known hydrolytic/thermal intermediate en route to bismuth (III) oxide. The subsequent mass loss at 326 °C (2.95%) is then attributable to the further dehydration of BiO(OH) to Bi_2O_3 ($2\ BiO(OH) \rightarrow Bi_2O_3 + H_2O$). A fourth event at 599 °C (3.47%) is ascribed to oxidative decomposition/combustion of occluded tetrapropylammonium (TPA^+) residues trapped within the host framework [51–53]. Finally, a 7.58% loss at 749 °C marks the onset of framework densification and partial collapse, driven by condensation of surface and defect silanol groups and concomitant dehydroxylation. Overall, these features show that SDA removal is effective but accompanied by crystallographic modifications consistent with the $Bi(OH)_3 \rightarrow BiO(OH) \rightarrow Bi_2O_3$ transformation pathway [46].

To assess thermal robustness, powder X-ray diffraction patterns of the as-synthesized sample (BiSi-1) and specimens calcined at 450 °C (BiSi-3), 550 °C (BiSi-4), and 750 °C (BiSi-5) (Fig. SF2, Supplementary Material). While full structural assignment of BiSi-3/4/5 is ongoing, the preliminary diffractograms corroborate successful SDA elimination and indicate that the material remains thermally stable up to approximately 750 °C, exhibiting no complete amorphization despite the onset of partial framework collapse at the highest temperature. Soxhlet extraction with a 90:10 (v/v) dichloromethane/ethanol mixture at 90 °C efficiently removed the organic structure-directing agent, yielding a material with increased specific surface area and larger pore diameter, as evidenced by N_2 adsorption–desorption analyses. This extracted sample is denoted BiSi-6; its FT-IR and N_2-sorption results are presented and discussed in the following section.

FT-IR and XANES/EXAFS

FT-IR spectra for the calcined specimens—BiSi-3 (450 °C), BiSi-4 (550 °C), and BiSi-5 (750 °C)—are presented in Supplementary Material (Fig. SF3). Figure 4 presents three FT-IR spectra: the as-synthesized solid (BiSi-1), the Soxhlet-extracted solid (BiSi-6; extracted with dichloromethane/ethanol 90:10, v/v, at 90 °C), and the corresponding Soxhlet extract (solution). In all cases, the spectral features are consistent with those reported for silicate frameworks [54, 55].

In the 200–1300 cm^{-1} region, bands arise from internal vibrations of tetrahedral TO_4 units (T=Si): a strong feature at 1119 cm^{-1} is assigned to ν_{as}(Si–O–Si), the 802 cm^{-1} band to ν_s(Si–O–Si) (often described as the stretching of isolated $(SiO_4)^{4-}$ units in silica-rich frameworks), and a low-frequency envelope near 469 cm^{-1} to δ(Si–O–Si) bending. A broad absorption around 3446 cm^{-1} reflects hydrogen-bonded O–H stretching. Signals from the organic structure-directing agent tetrapropylammonium (TPA^+)—notably 1381 and 1442 cm^{-1} (C–H deformations) and 2959 cm^{-1} (C–H stretching)—are present only in the as-made solid and are absent after Soxhlet extraction and calcination, confirming efficient template removal [52, 53]. Although a band near 1444 cm^{-1} is sometimes attributed to ν_{as}(Bi–Cl) in BiOCl, that assignment is inapplicable here (no chloride in synthesis); the coincident intensity arises from TPA^+ vibrations rather than Bi–Cl bonding. Likewise, diagnostic Bi–O–Si stretches often cited near 947 and 551 cm^{-1} (the former associated with metal substitution at tetrahedral sites) are not resolved, which argues against extensive Bi substitution into the silicate framework [56]. Instead, the overlap of the 469–490 cm^{-1} region with reported Bi–O–Bi modes of distorted [BiO_6] polyhedra—together with our thermal pathway $Bi(OH)_3 \rightarrow BiO(OH) \rightarrow Bi_2O_3$—supports a picture in which bismuth resides predominantly in extra-framework Bi-oxo environments intimately associated with a silica-rich host [21, 57].

X-ray absorption spectroscopy corroborates this assignment. Bi L_3-edge XANES (13.418 keV), processed in ATHENA for background removal and normalization, is reproducible across three probe positions for each sample (BiSi-1 and BiSi-2), indicating spectral homogeneity (Fig. 5). With the Bi foil calibrated to 13.418 keV, the sample edges are shifted by + 2 eV to 13.420 ± 0.2 keV, and the white-line intensity is clearly enhanced relative to the metal. The combination of a small positive edge shift and an intensified white line is diagnostic of Bi^{3+} in an oxide-like environment, excluding any significant Bi^0 contribution. A weak post-edge resonance is observed near ~ 13.44–13.46 keV; scans were deliberately truncated below the Br K-edge (13.474 keV) to avoid spectral contamination, and no Bi–Br signatures are detected.

To access the extended structure without Br overlap, Bi L_1-edge (16.385 keV) XANES/EXAFS was collected. As expected for the L_1 edge, the EXAFS amplitude is weaker than at L_3, so a reduced k-range was analyzed. The L_1 XANES again shows a stronger white line than the foil, confirming oxidized Bi (Fig. 6). The phase-uncorrected Fourier transforms $|\chi(R)|$ display

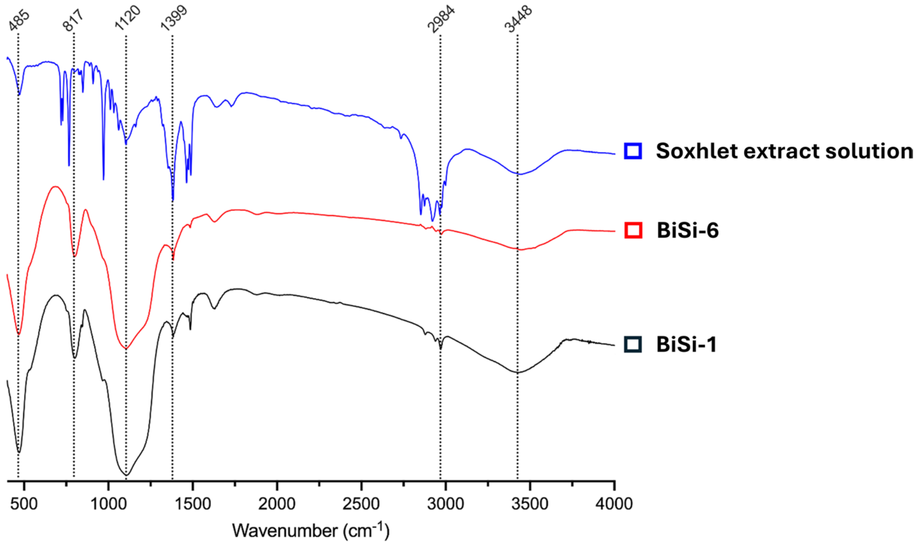

Figure 4 FT-IR spectra of (i) the as-synthesized solid (BiSi-1), (ii) the Soxhlet-extracted solid (BiSi-6; dichloromethane/ethanol, 90:10 v/v, 90 °C), and (iii) the corresponding Soxhlet extract (solvent phase) containing the removed structure-directing agent (TPA^+).

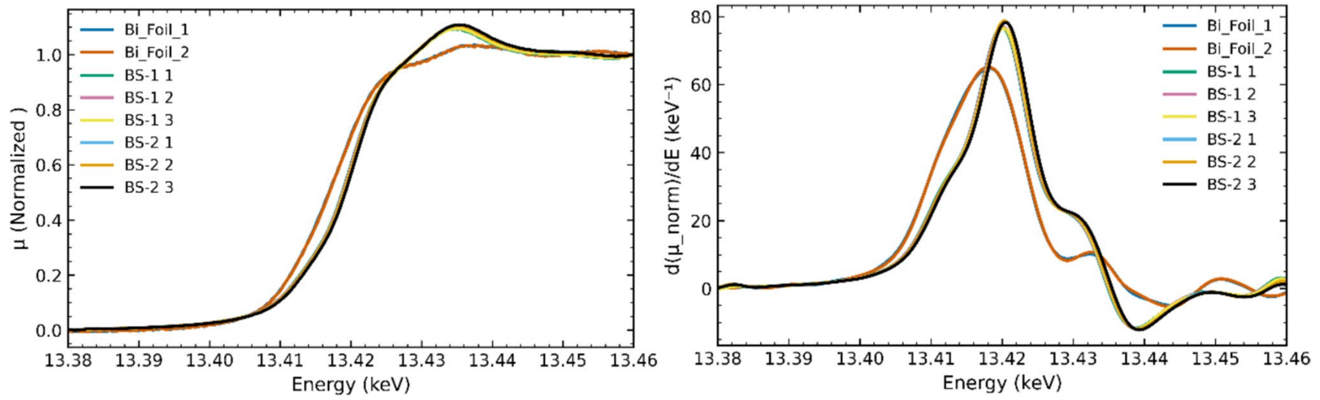

Figure 5 Bi L_3-edge XANES. The left panel shows normalized μ(E) spectra of BiSi-1 and BiSi-2 (averaged over three positions each) compared with Bi foil, while the right panel presents the first derivative, dμ/dE, revealing a slight positive edge shift for BiSi-1 and BiSi-2.

a dominant first-shell peak at 1.6–1.8 Å, assigned to Bi–O scattering (corresponding, after phase-shift correction, to a real-space Bi–O distance of approximately 2.1–2.3 Å typical of distorted Bi–O polyhedra). Higher-*R* features are weak and strongly damped in both BiSi-1 and BiSi-2, in sharp contrast to the foil, which exhibits intense Bi–Bi correlations beyond 4–5 Å; this rules out metallic Bi and indicates a locally ordered but medium-range-disordered Bi–O network consistent with nanocrystalline/porous or layered architectures. Notably, the $|\chi(R)|$ profiles of BiSi-1 and BiSi-2 overlay within experimental uncertainty, showing that the first Bi–O coordination shell is conserved already at 12 h aging; differences seen by XRD and N_2 sorption (improved crystallinity, higher surface area/pore volume with prolonged aging) therefore reflect long-range ordering and textural evolution, not changes in the immediate Bi–O environment.

Taken together, FT-IR (silica-rich framework, removable TPA^+, absence of clear Bi–O–Si framework markers), XANES (Bi in the + 3 oxidation state with oxide-like electronic structure), and EXAFS (pronounced Bi–O first shell, strongly damped medium-/long-range order, no Bi–Bi or Bi–halide coordination) converge on a coherent model: Bi is predominantly trivalent and oxygen-coordinated in extra-framework Bi-oxo motifs embedded within an anisotropic, silica-rich host, with long-range order that improves upon aging but a conserved local Bi–O environment across synthesis protocols. This spectroscopic picture is fully

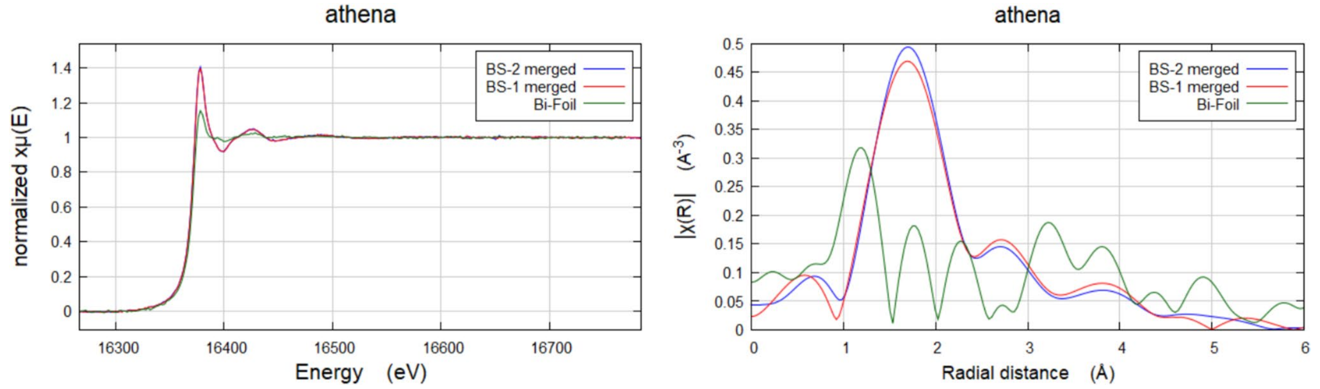

Figure 6 Bi L_1-edge XANES/EXAFS (merged datasets). The left panel shows normalized μ(E) spectra of BiSi-1 and BiSi-2 (merged, processed in ATHENA) compared with a Bi foil. The right panel presents the magnitude of the phase-uncorrected Fourier transform |χ(R)| from the k-weighted EXAFS, where a dominant first-shell peak at ~ 1.6–1.8 Å indicates Bi–O coordination. Higher-R contributions are strongly damped relative to the foil, and BiSi-1 and BiSi-2 overlay closely, with no evidence for metallic Bi or Bi–Br coordination.

consistent with the thermal transitions observed by TGA/DTG.

N_2 adsorption measurements

Nitrogen adsorption/desorption measurements of the bismuth silicate samples were performed at − 196 °C, using a Micromeritics ASAP 2020 Plus static volumetric analyzer. All the adsorption data concerning the porosities of the samples, including the BET surface areas, micro- and mesoporous volumes, and pore size distributions, obtained using different models, were provided by the workstation of the ASAP 2020 Plus analyzer. All the powders showed pores in the mesopore size range and a small pore volume in the micropore range. The BiSi-2 and BiSi-5 samples presented very low pore volume values and an isotherm in the form of a 45° inclination line, typical of materials with little or no porosity. The isotherms of BiSi-1, BiSi-3, BiSi-4, BiSi-6, to materials with pores in the mesopore range, although they do not have exactly the same appearance as the type IV isotherm, according to the classification of the International Union of Pure and Applied Chemistry (IUPAC), it is possible to state that the respective isotherms refer to mesoporous materials with a hysteresis loop closer to the H1 type, suggesting mesoporosity, with pore condensation at high pressure. This was indicated by two branches of the isotherm that were almost parallel, which is a type of hysteresis normally associated with porous materials constituted by rigid agglomerates of spherical particles with uniform size. Some significant changes in these isotherms could be observed, such as a systematic decrease in the amount of nitrogen adsorbed with increase of the calcination temperature from 450 to 750 °C, indicating a reduction in pore volume, with a consequent reduction in the specific surface area value. After calcination at 750 °C, the pores were practically eliminated and the appearance of the isotherm shifted from mesoporous to non-porous (type III). The insets in each graph in Fig. 7 show pore size distribution curves for the bismuth silicates, obtained using the BJH model. All the average pore sizes were in the mesopore range, 22 with BiSi-1, BiSi-4, and BiSi-5 having very small pore volumes (Table 1). Comparison of the pore size distribution curves for the powders obtained after calcination at the three temperatures showed that increase of the calcination temperature resulted in a reduction of the total pore volume. Increasing the temperature from 450 to 550 °C resulted in elimination of most of the pores smaller than 100 Å, so the average pore diameter increased from 63 to 120 Å. Further increase of the calcination temperature to 750 °C practically eliminated the pores, reducing the area value to 27 $m^2 g^{-1}$. The highest specific surface area and pore volume values were observed for the powder obtained after Soxhlet extraction ($S = 310$ $m^2 g^{-1}$ and pore volume of 0.36 $cm^3 g^{-1}$), showing that this was an effective method for obtaining a porous bismuth silicate with high specific surface area, with efficient removal of the organic template, without any need for thermal treatment (which would result in the elimination of pores and reduction of the surface area). From comparison of the BiSi-1 and BiSi-2 silicates, which differed only in terms of aging time, it could be concluded that increasing the aging time from 12 to 24 h resulted in greater crystallization and an increase in pore volume from 0.065 to 0.21 $cm^3 g^{-1}$, with a consequent increase in the specific surface area from 62 to 149 $m^2 g^{-1}$. The BJH pore size distributions of the BiSi-1, BiSi-3, BiSi- 4, and BiSi-6 samples were in the range 5.5–12.2 nm, confirming the presence of hierarchical mesopores in these bismuth silicates. It should be noted that the mesopore volumes of BiSi-1 (0.21 $cm^3 g^{-1}$), BiSi-3 (0.20 $cm^3 g^{-1}$), BiSi-4 (0.14 $cm^3 g^{-1}$), and BiSi-6 (0.36 $cm^3 g^{-1}$) were higher than those of conventional zeolites such as zeolite Beta (0.09 $cm^3 g^{-1}$) and ZSM-5 (0.05 $cm^3 g^{-1}$) [58, 59].

SEM and TEM measurements

Figure 8 shows a representative micrograph (5 kV, × 8000; scale bar 1 μm) of the BiSi-1. It shows micron-scale aggregates composed of submicron granular features (tens to a few hundreds of nanometers) with occasional thin platelet/flake-like fragments. The surface appears rough and porous at the sub-micron level. The observed multiscale texture is, however, compatible with the mesoporosity inferred from N_2-sorption. SEM of materials calcined at 450 °C (BiSi-3), 550 °C (BiSi-4), and 750 °C (BiSi-5) is shown in Supplementary Material (Fig. SF4), and the morphology is similar to the BiSi-1. Qualitative composition obtained by EDS shows the spectrum indicates Bi, Si, and O as the major elements, consistent with a bismuth silicate. Cu lines are attributed to the mount/stub and are considered extrinsic. SEM–EDS was inconclusive for Br owing to (i) the low expected Br content (below the EDS detection limit in a Bi-rich matrix) and (ii) line

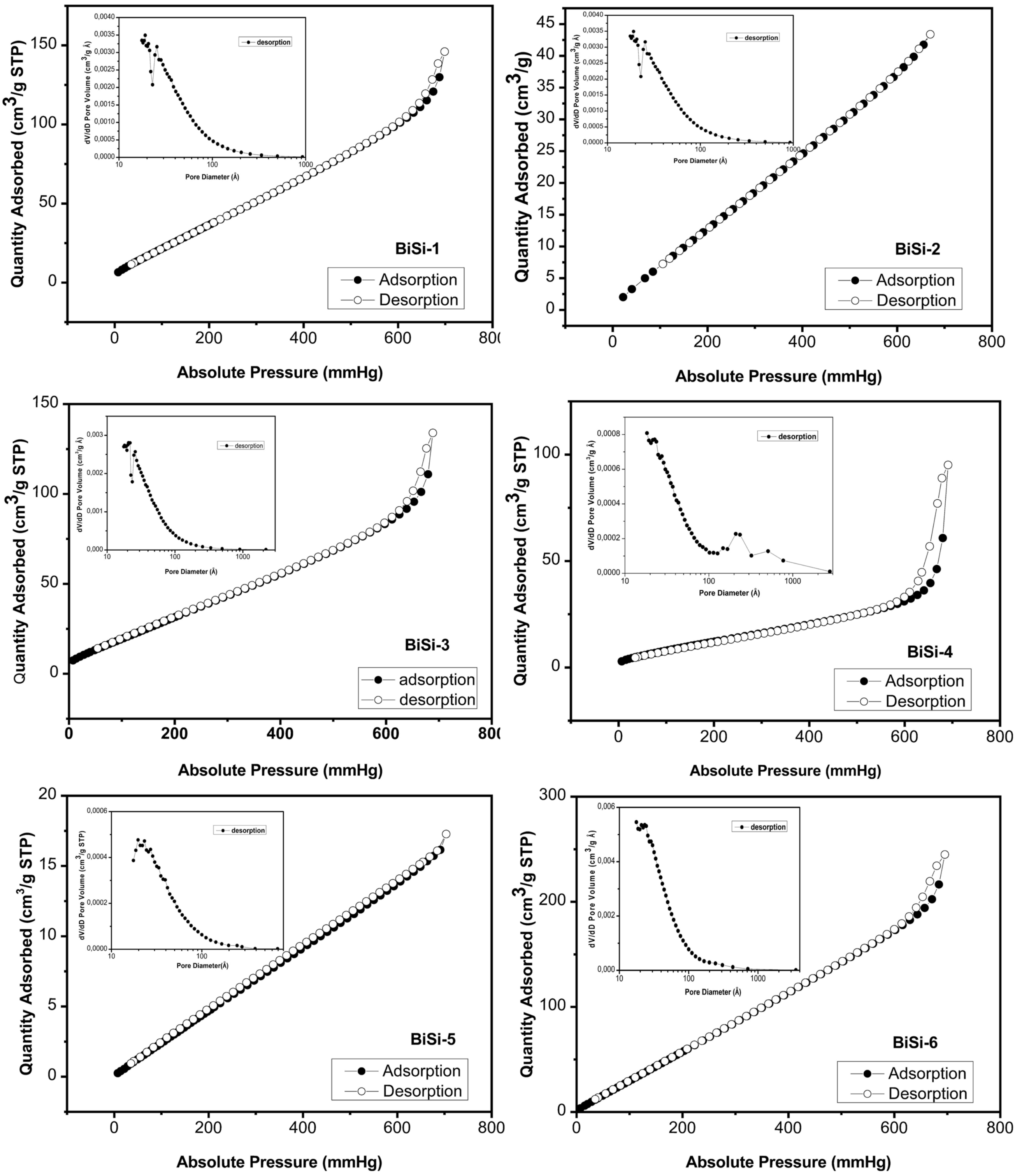

Figure 7 N_2 adsorption–desorption isotherms at 77 K and BJH pore-size distributions for bismuth silicate samples. Samples BiSi-1, BiSi-3, BiSi-4 and BiSi-6 display type-IV, H1-like isotherms indicative of mesoporosity, BiSi-2 and BiSi-5 exhibit low, near-linear uptake with no evident hysteresis, consistent with negligible microporosity. Calcination decreases uptake and pore volume, while Soxhlet extraction (BiSi-6) affords the highest surface area and mesopore volume.

Table 1 Textural parameters of the bismuth silicate samples, obtained from N_2 absorption and desorption measurements

Sample	S ($m^2\ g^{-1}$)	$V_{mesopores}$ ($cm^3\ g^{-1}$)	$\Phi_{mesopores}$ (Å)	$V_{micropores}$ ($cm^3\ g^{-1}$)	$\Phi_{micropores}$ (Å)
BiSi-1 (24 h aging)	149	0.21	55	0.039	1.1
BiSi-2 (12 h aging)	62	0.065	43	0.011	1.1
BiSi-3 (calcined at 450 °C)	118	0.20	63	0.034	1.0
BiSi-4 (calcined at 550 °C)	44	0.14	122	0.015	1.0
BiSi-5 (calcined at 750 °C)	27	0.023	45	0.004	1.2
BiSi-6 (Soxhlet extraction)	310	0.36	54	0.054	1.2

S, surface area determined by BET theory; $V_{mesopores}$, mesopore volume determined by BJH theory; $\Phi_{mesopores}$, mesopore size; $V_{micropores}$, micropore volume determined by the Horvath–Kawazoe method; $\Phi_{micropores}$, micropore size

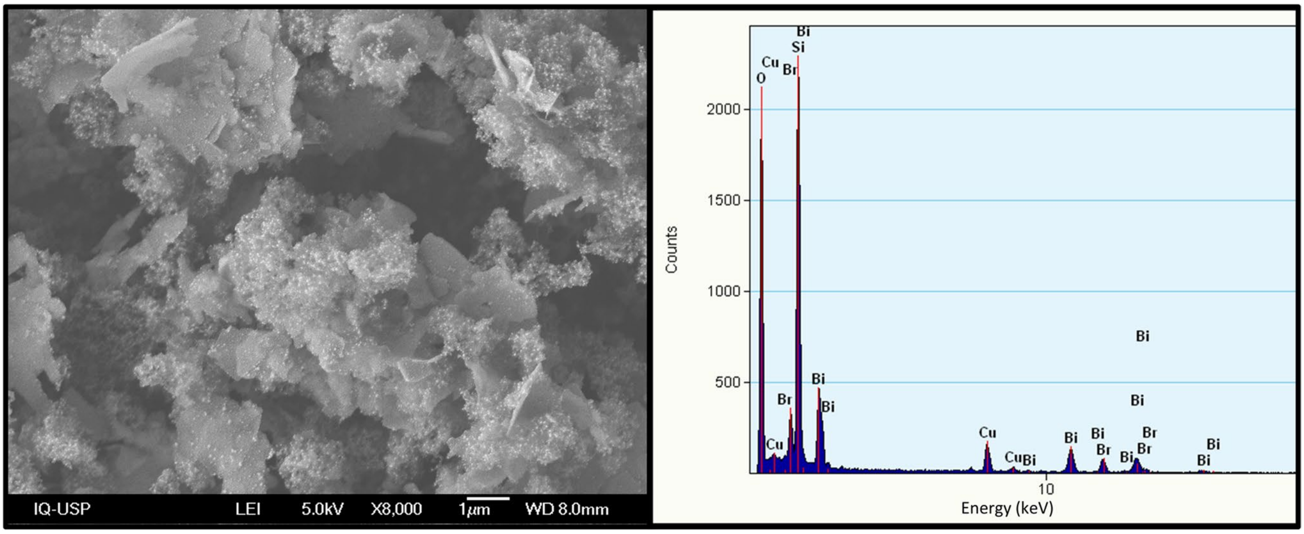

Figure 8 SEM micrograph (5 kV, × 8000; scale bar = 1 µm) and accompanying EDS for the as-synthesized bismuth silicate (BiSi-1). The powder forms micron-scale aggregates constructed from submicron granular domains (≈10^2–10^3 nm) with occasional thin platelet/flake-like fragments. Surfaces are rough and appear porous at the sub-micron scale. EDS identifies Bi, Si, and O as the principal elements; while minor Cu peaks arise from the specimen holder.

overlap between Br K (Kα 11.92, Kβ 13.29 keV) and Bi L (Lα 10.84, Lβ_1 ~ 13.02 keV) emissions.

TEM of BiSi-1 (Fig. 9) confirms that the powder consists of nanocrystalline bismuth–silicate domains, including plate-like crystallites, assembled into submicrometric aggregates (as also observed by SEM). The HRTEM lattice spacings corroborate the XRD d-values, while the mixed SAED pattern—characterized by concentric Debye–Scherrer rings together with discrete Bragg reflections—indicates the coexistence of randomly oriented nanograins and locally oriented lamellae, consistent with the highly anisotropic, layered structure proposed for BiSi-1. Panel A shows well-resolved lattice fringes extending over tens of nanometers, evidencing crystalline domains. From the scale bar (nm range), the interfringe distance is in the ~ 0.27–0.32 nm window, consistent with the strongest XRD spacings of BiSi-1 ($d \approx 0.31, 0.29, 0.28$ nm corresponding to $2\theta \approx 28$–$33°$ with Cu Kα). Pattern B displays concentric rings composed of discrete spots, typical of polycrystalline aggregates of randomly oriented nanocrystallites; the ring radii (not indexed here) match the principal d-spacings seen by XRD (≈3.60, 3.19, 3.12, 2.87, 2.77, 2.71 Å). Pattern C shows a sharp, spotty array characteristic of a single crystal or a few well-aligned crystallites along a low-index zone axis; the near-rectangular symmetry of the reciprocal lattice is compatible with an orthorhombic projection. The absence of a pronounced diffuse halo indicates little amorphous content in the probed region.

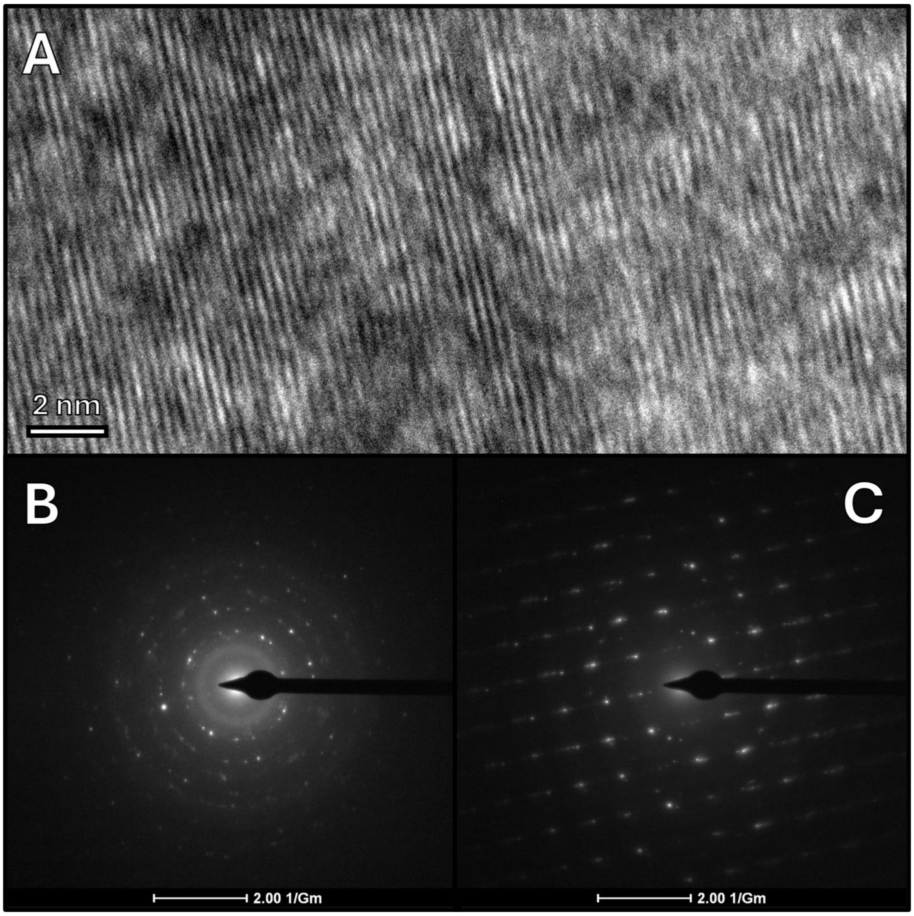

Figure 9 TEM/HRTEM and SAED of BiSi-1. Nanocrystalline bismuth-silicate domains assemble into submicrometric aggregates. (A) HRTEM shows lattice fringes ($d \approx 0.27$–0.32 nm) matching the strongest PXRD reflections; (B–C) SAED displays concentric rings from randomly oriented nanograins and a spotty pattern from oriented domains, compatible with an orthorhombic projection; weak diffuse scattering indicates low amorphous content.

Representative TEM/SAED data for the calcined samples BiSi-4 (550 °C), and BiSi-5 (750 °C)—are provided in Supplementary Material (Figs. SF5–SF6). HRTEM of BiSi-3 and BiSi-4 shows that both materials remain nanocrystalline, but display a predominantly polycrystalline, less strongly oriented texture than the as-synthesized BiSi-1. Low-contrast regions with poorly resolved periodicity occur adjacent to ordered domains, consistent with defect-rich and/or partially disordered silica-rich areas generated during OSDA removal and dehydroxylation. Correspondingly, SAED evolves from the mixed spots-on-rings pattern of BiSi-1—reflecting coexisting aligned lamellae and randomly oriented nanograins—to largely continuous Debye–Scherrer rings after calcination, indicating diminished long-range order and a broader orientation distribution. This microstructural evolution accords with the thermal history (template removal and partial framework rearrangement) and with diffraction/XANES-EXAFS evidence that the local Bi–O coordination is retained despite reduced medium- to long-range crystallinity.

For BiSi-5 (750 °C), HRTEM reveals extended regions with weak or only short-range periodicity alongside crystallites exhibiting clear lattice fringes. The powder therefore comprises crystalline Bi–O–Si domains embedded in a more disordered, silica-rich matrix. These trends are consistent with TGA/DTG (final mass loss near 750 °C from silanol condensation) and N_2-sorption (loss of mesoporosity), indicating densification and partial collapse of the porous network at high temperature while preserving the first-shell Bi–O environment.

Magic-angle spinning (MAS) solid-state (SS) NMR

Figure 10 shows the ^{1}H-^{29}Si cross-polarization magic angle spinning (^{1}H-^{29}Si CPMAS) spectrum of an as-made bismuth silicate sample (BiSi-1), using a cross-polarization time (CT) of 1 ms. The spectrum was fitted using three Gaussian functions peaking at − 113.2 ppm, − 102.5 ppm, and − 92 ppm, with percentage areas (relative to the total spectral area) of 47%, 44%, and 9%, respectively. When the cross-polarization time was increased to 5 ms, the percentage areas changed to 61%, 34%, and 4%, while the peak positions remained unchanged.

As is well known, the ^{1}H-^{29}Si CPMAS intensity varies with the cross-polarization time, according to the quantity of neighbor ^{1}H nuclei, presenting an initial build-up until a maximum is reached, followed by a decrease due to relaxation of the spins (so-called $T_{1\varrho}$ relaxation). Because the rate of the initial build-up with the cross-polarization time is proportional to the local ^{1}H density, acquiring ^{1}H-^{29}Si CPMAS spectra with different cross-polarization times is useful for identifying ^{29}Si nuclei close to different numbers of ^{1}H, providing information complementary to the typical chemical shifts (peak positions), which concerns the identification of the number of bridging oxygens of ^{29}Si. The chemical shifts at − 113.2 ppm, − 102.5 ppm, and − 92 ppm (Fig. 11) were consistent with the presence of Q_4, Q_3, and Q_2 silanol end groups [60]. This was further confirmed by the observation that the relative area of the − 113.2 ppm peak increased from 47 to 61%, while the area of the signal at − 102.5 ppm decreased from 44 to 34%, and the area of the − 92.0 ppm peak decreased from 9 to 4%. This behavior showed that for CT times varying from 1 to 5 ms, the − 113.2 ppm signal was still in the initial build-up (less neighbor ^{1}H), while the intensities of the − 102.5 ppm and 92 ppm peaks had already decreased, due to $T_{1\varrho}$ relaxation, consistent with a local environment richer in ^{1}H. In addition, the − 102.5 ppm signal presented a smaller area reduction than the -92 ppm signal, suggesting that the former had less neighboring ^{1}H. In summary, the assignment of the signals to Q_4, Q_3, and Q_2 silanol end groups was in full agreement with the intensity changes observed in the ^{1}H-^{29}Si CPMAS spectra for cross-polarization times of 1 and 5 ms.

To obtain a more quantitative assessment of the relative amounts of the Q_4, Q_3, and Q_2 silanol end groups in the sample, a single pulse excitation spectrum under MAS (SPEMAS) was acquired, with recycle delay of 20 s. Under this condition, the spectra were more quantitative, so the relative peak areas obtained from the fitting provided a good estimation of the relative amounts of the Q_4, Q_3, and Q_2 silanol end groups in the sample. However, despite requiring a substantially longer measuring time than the ^{1}H-^{29}Si CPMAS, the spectra had the worst signal-to-noise ratios, making the fitting with the peak positions as free parameters unreliable. Therefore, the Gaussian peak positions

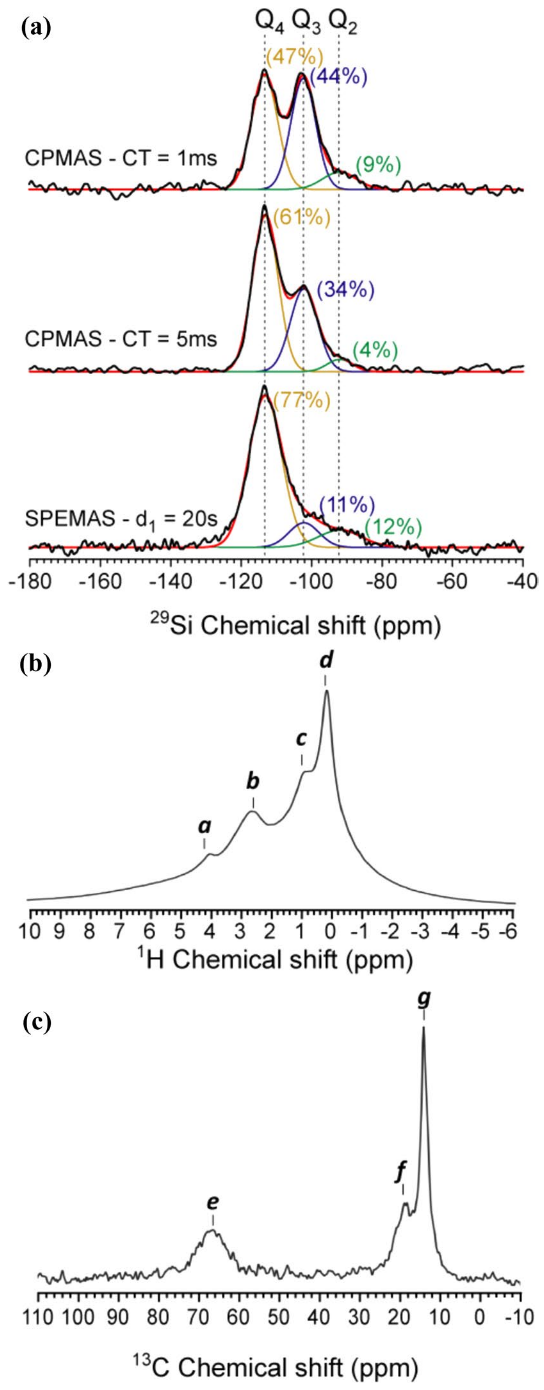

Figure 10 Magic angle spinning solid-state NMR spectra for the as-made bismuth silicate sample (BS-1). **a** Top: ^{1}H-^{29}Si cross-polarization under magic angle spinning (CPMAS) spectrum acquired with cross-polarization time (CT) of 1 ms. Also shown is the fitting of the spectrum using three Gaussian lines, with positions and area percentages indicated. Middle: CPMAS spectrum with contact time of 5 ms. Bottom: Single pulse excitation under magic angle spinning (SPEMAS) spectrum acquired with recycle delay (d_1) of 20 s. The fitting of the spectrum was performed using three Gaussian lines at the same positions as those shown in the preceding spectra, resulting in the percentage areas indicated. **b** ^{1}H EASY spectrum of the as-made bismuth silicate sample. c) ^{13}C CPMAS spectrum of the as-made bismuth silicate sample.

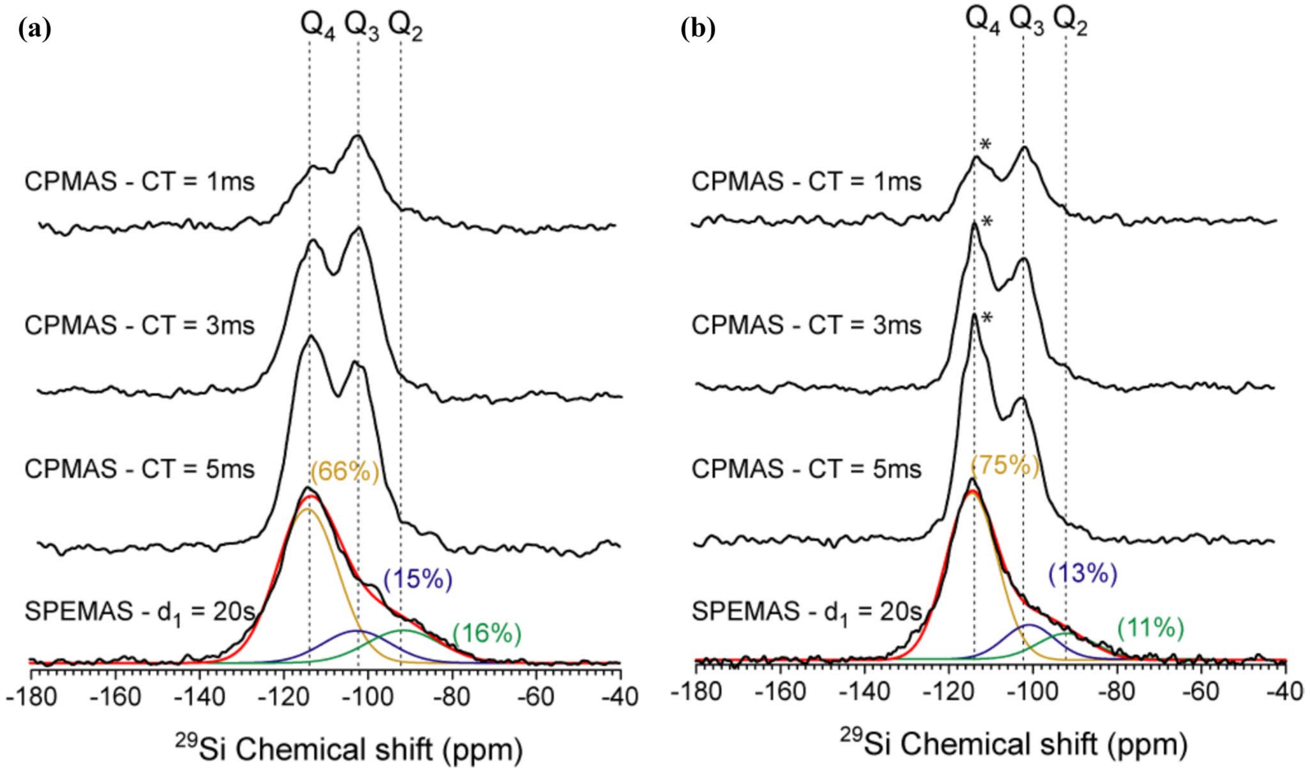

Figure 11 ^{29}Si magic angle spinning solid-state NMR spectra of aged bismuth silicate samples. **a** Sample with 12 h of aging (BiSi-2). Top and middle: ^{1}H-^{29}Si CPMAS spectra acquired with cross-polarization times (CT) of 1 and 5 ms. Bottom: ^{1}H SPEMAS spectrum acquired with a long relaxation delay (20 s), together with the Gaussian fits considering the Q_2, Q_3, and Q_4 silanol end groups. The percentages for the groups are indicated. **b** Same as **a** for the sample with 24 h of aging (BiSi-1).

obtained from the CPMAS spectrum were fixed, with only the relative areas as free parameters in the fitting. With this procedure, the relative amounts of Q_4, Q_3, and Q_2 silanol end groups were estimated as 77%, 11%, and 12%, respectively, revealing a considerable excess of Q_4 groups, compared to Q_3 and Q_2, with Q_1 apparently being negligible.

In addition to ^{29}Si NMR, ^{1}H MAS and ^{13}C CPMAS spectra were acquired at 25 kHz (Fig. 11). The ^{1}H spectrum showed signals at around 1.0 ppm (peak *d*) and 1.7 ppm (peak *c*), indicating the presence of organic solvents. There was also a signal at around 3.4 ppm (peak *b*), probably arising from terminal Si–OH groups in exchange with physisorbed water. A smaller signal at 4.75 ppm (peak *a*) was related to sample moisture. The broad peaks in the spectrum meant that minor signals might be overlooked. The signal at 1.0 ppm had a weak shoulder at around 1.1 ppm, which could have been related to unbound SiOH terminations. However, the apparent moisture level of the sample did not support the presence of unbound hydroxyl groups, showing the clear presence of SDA in the as-made product. The ^{1}H MAS spectra also appeared to be dominated by these compounds. The ^{13}C spectra showed signals that confirmed the presence of organic solvents from the synthesis.

The ^{29}Si NMR spectra of the bismuth silicates prepared using TPA.Br and aging times of 12 (BiSi-2) and 24 h (BiSi-1) are shown in Fig. 12. The ^{1}H-^{29}Si CPMAS and SPEMAS spectra revealed the presence of Q_4, Q_3, and Q_2 silanol end groups, with a considerable excess of Q_4 groups. However, comparing the ^{1}H-^{29}Si CPMAS spectra of the two samples, there was the appearance of a sharper signal structure (marked with an asterisk) in the spectrum for the sample prepared with aging for 24 h. This could have resulted from an increase in local structural ordering, in agreement with the appearance of the highest crystalline phase after 24 h of aging, as shown by the X-ray diffraction results (Fig. 1).

The effect of sample calcination on the ^{29}Si NMR spectrum is shown in Fig. 12. It can be seen that there was a progressive decrease of the signal-to-noise ratio of the ^{1}H-^{29}Si CPMAS spectrum with higher calcination temperature. This reflected the loss of hydrogen

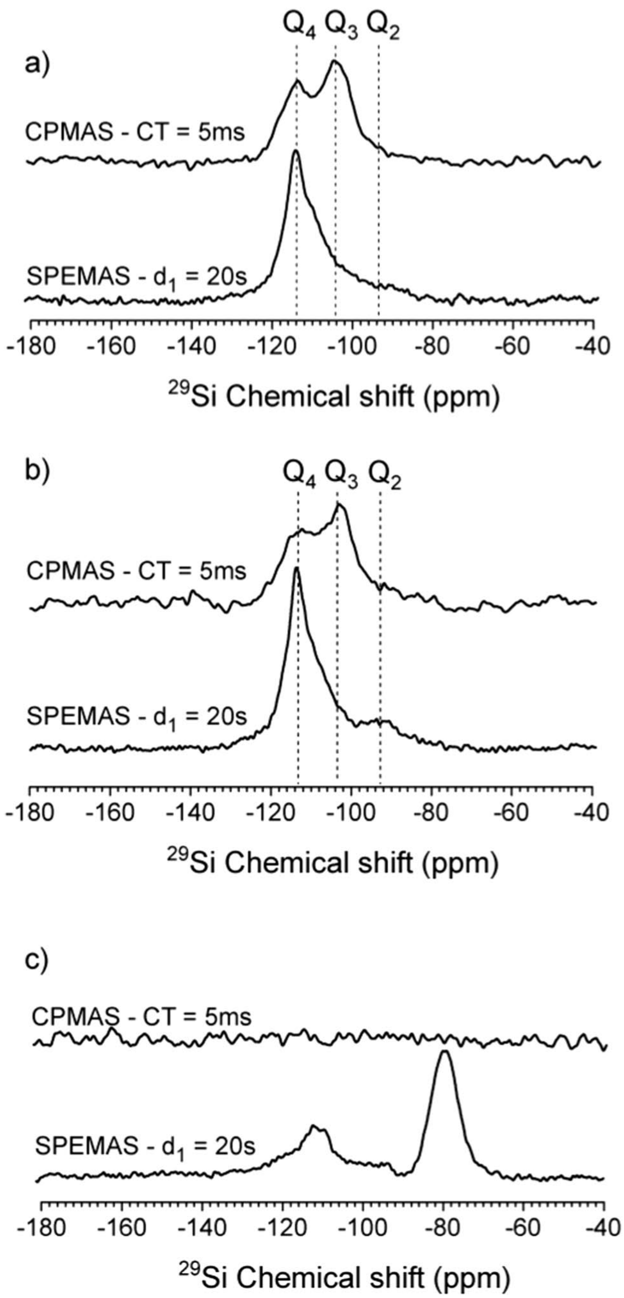

Figure 12 ^{1}H-^{29}Si CPMAS and ^{29}Si SPEMAS spectra of the bismuth silicate samples calcined at **a** 450 °C (BiSi-3), **b** 550 °C (BiSi-4), and **c** 750 °C (BiSi-5).

by the calcination, which decreased the efficiency of the ^{1}H-^{29}Si cross-polarization process. In fact, for the calcination temperature of 750 °C, no ^{1}H-^{29}Si CPMAS signal at all was detected, pointing to the lack of hydrogen close to ^{29}Si in the sample. Interestingly, the ^{29}Si SPEMAS spectra were similar for calcination temperatures of 450 and 550 °C, but a drastic change was observed for calcination at 750 °C, showing that the loss of hydrogen was accompanied by a major change in the local structure of the ^{29}Si groups, in agreement with the X-ray diffraction and FT-IR results.

Conclusions

We report the hydrothermal synthesis of a new bismuth silicate (BiSi-1), obtained using tetrapropylammonium bromide (TPA·Br) as the organic structure-directing agent. While both TPA·Br and polydiallyldimethylammonium chloride (PDADMAC) were investigated, only TPA·Br yielded a crystalline Bi–silicate phase, underscoring the critical role of OSDA selection in directing bismuth silicate crystallization.

Comprehensive physicochemical characterization (XRD, HRTEM/SAED, solid-state NMR, XANES/EXAFS, ICP–OES, TGA/DTG, and N_2 sorption) establishes BiSi-1 as a nanocrystalline, anisotropic material with a silica-rich framework, stable Bi^{3+}–O coordination, and tunable porosity. The combination of framework anisotropy, thermal robustness, and accessible textural properties highlights BiSi-1 as a promising candidate for heterogeneous catalysis and environmental remediation. These findings expand the structural landscape of Bi–silicates and motivate further studies toward full crystallographic solution and operando investigations linking structure to function.

Acknowledgements

This research was supported by the following Brazilian funding agencies: The São Paulo Research Foundation (FAPESP) under grant numbers #2019/01858-5 and #2022/16214-9 (J. G. N.), and #2018/19251-7 (I. C. C.); the National Council for Scientific and Technological Development (CNPq) under grant numbers #317030/2021-3 and #406761/2013-2 (J. G. N.); and the Coordination for the Improvement of Higher Education Personnel (CAPES) through doctoral fellowships #88887.513909/2020-00 (E. P. C.) and #88887.661419/2022-00 (G. P. G.). The authors extend their gratitude to the Structural Characterization Laboratory (LCE/Dema/UFSCar) and the Analytical Center of the Institute of Chemistry (CA/IQ/USP) for providing access to research facilities. We also acknowledge the Helmholtz-Zentrum Berlin für Materialien und

Energie for granting beamtime at the synchrotron radiation facility.

Author contributions

Erick Paiva Cancella contributed to syntheses, spectroscopy data acquisition, figures preparation; Guilherme de Paula Guarnieri contributed to syntheses, spectroscopic data analysis, figures preparation, original draft; Nader de Sousa Amadeu contributed to data acquisition and formal analyses of solid-state NMR data; Martin Radtke contributed to data acquisition and formal analyses of XANES and EXAFS data; Eduardo Ribeiro de Azevedo contributed to data acquisition and formal analyses of solid state NMR data; Rodrigo Henrique Garcia contributed to NMR data acquisition; Ivana Conte Cosentino contributed to data acquisition and formal BET-N_2 analyses; Yvonne Primerano Mascarenhas contributed to single crystal and X-ray powder diffraction analysis; Jose Geraldo Nery contributed to writing—original draft, formal analysis, data interpretation, supervision, review and editing, project administration.

Funding

Fundação de Amparo à Pesquisa do Estado de São Paulo, 2019/01858-5, José Geraldo Nery, 2022/16214-9, José Geraldo Nery, 2018/19251-7,Ivana Conte Cosentino, Conselho Nacional de Desenvolvimento Científico e Tecnológico,317030/2021-3, José Geraldo Nery, 406761/2013-2, José Geraldo Nery, Coordenação de Aperfeiçoamento de Pessoal de Nível Superior, 88887.513909/2020-00, Erick Paiva Cancella,88887.661419/2022-00, Guilherme de Paula Guarnieri

Data availability

Data will be made available upon reasonable request to the corresponding author.

Declarations

Conflict of interest The authors declare that they have no known competing financial interests or personal relationships that could have appeared to influence the work reported in this paper.

Ethical approval Not applicable.

Supplementary Information The online version contains supplementary material available at https://doi.org/10.1007/s10853-025-11732-6.

References

[1] Feliczak-Guzik A (2018) Hierarchical zeolites: synthesis and catalytic properties. Microporous Mesoporous Mater 259:33–45. https://doi.org/10.1016/j.micromeso.2017.09.030

[2] Dusselier M, Davis ME (2018) Small-pore zeolites: synthesis and catalysis. Chem Rev 118:5265–5329. https://doi.org/10.1021/ACS.CHEMREV.7B00738/ASSET/IMAGES/MEDIUM/CR-2017-007389_0047.GIF

[3] Chukanov NV, Pekov IV, Rastsvetaeva RK (2004) Crystal chemistry, properties and synthesis of microporous silicates containing transition elements. Russ Chem Rev 73:205–223. https://doi.org/10.1070/RC2004v073n03ABEH000825

[4] Chukanov NV (2005) Heterosilicates with tetrahedral-octahedral frameworks: mineralogical and crystal-chemical aspects. Rev Mineral Geochem 57:105–143. https://doi.org/10.2138/rmg.2005.57.4

[5] Rocha J (2005) Microporous mixed octahedral-pentahedral-tetrahedral framework silicates. Rev Mineral Geochem 57:173–201. https://doi.org/10.2138/rmg.2005.57.6

[6] Odularu AT (2020) Bismuth as smart material and its application in the ninth principle of sustainable chemistry. J Chem 2020:1–15. https://doi.org/10.1155/2020/9802934

[7] Sivasubramanian P, Chang J-H, Nagendran S et al (2022) A review on bismuth-based nanocomposites for energy and environmental applications. Chemosphere 307:135652. https://doi.org/10.1016/j.chemosphere.2022.135652

[8] Ollevier T (2013) New trends in bismuth-catalyzed synthetic transformations. Org Biomol Chem 11:2740. https://doi.org/10.1039/c3ob26537d

[9] Mato M, Cornella J (2024) Bismuth in radical chemistry and catalysis. Angew Chem Int Ed Engl. https://doi.org/10.1002/anie.202315046

[10] Meng F, Ling Y, Li X et al (2023) Preparation of Bi2O3 modified ZSM-5 with photo-deposition method and its application in pyridine base synthesis. Microporous Mesoporous Mater 348:112386. https://doi.org/10.1016/j.micromeso.2022.112386

[11] Dumitriu D (2003) BiOx clusters occluded in a ZSM-5 matrix: preparation, characterization, and catalytic behavior in liquid-phase oxidation of hydrocarbons. J Catal 219:337–351. https://doi.org/10.1016/S0021-9517(03)00216-1

[12] Romanov AN, Serykh AI, Haula EV et al (2022) NIR photoluminescence of ZSM-5 and mordenite zeolites, containing low-valence bismuth exchange cations. Microporous Mesoporous Mater 336:111875. https://doi.org/10.1016/j.micromeso.2022.111875

[13] Zhao Y, Clément S, Veremeienko V et al (2019) High-pressure, high temperature insertion of bismuth in the siliceous zeolite silicalite-1. Solid State Sci 97:106001. https://doi.org/10.1016/j.solidstatesciences.2019.106001

[14] Tian Z, Chee T-S, Meng R et al (2022) Incipient wetness impregnation to prepare bismuth-modified all-silica beta zeolite for efficient radioactive iodine capture. Environ Funct Mater 1:92–104. https://doi.org/10.1016/j.efmat.2022.05.006

[15] Wang F, Qu D, Wang S et al (2022) Bismuth-decorated beta zeolites catalysts for highly selective catalytic oxidation of cellulose to biomass-derived glycolic acid. Int J Environ Res Public Health 19:16298. https://doi.org/10.3390/ijerph192316298

[16] Sun H-T, Sakka Y, Shirahata N et al (2013) NMR, ESR, and luminescence characterization of bismuth embedded zeolites Y. J Phys Chem C Nanomater Interfaces 117:6399–6408. https://doi.org/10.1021/jp401861c

[17] Sun H-T, Matsushita Y, Sakka Y et al (2012) Synchrotron x-ray, photoluminescence, and quantum chemistry studies of Bismuth-embedded dehydrated Zeolite Y. J Am Chem Soc 134:2918–2921. https://doi.org/10.1021/ja211426b

[18] Sun H, Hosokawa A, Miwa Y et al (2009) Strong ultrabroadband near-infrared photoluminescence from bismuth-embedded zeolites and their derivatives. Adv Mater 21:3694–3698. https://doi.org/10.1002/adma.200900573

[19] Hamoud HI, Douma F, Lafjah M et al (2022) Size-dependent photocatalytic activity of silver nanoparticles embedded in ZX-Bi zeolite supports. ACS Appl Nano Mater 5:3866–3877. https://doi.org/10.1021/acsanm.1c04484

[20] Sun H, Han F, Sun L et al (2022) Highly reactive methyl group drives selective catalytic reduction of NOx by methanol on bismuth oxide nanoparticle implanted FER zeolite. Appl Catal B 318:121883. https://doi.org/10.1016/j.apcatb.2022.121883

[21] Samadi-Maybodi A, Masoomeh Pourali S (2013) Microwave-assisted aging synthesis of bismuth modified zeolite-P microspheres via BiOCl nanoflake transformation. Microporous Mesoporous Mater 167:127–132. https://doi.org/10.1016/j.micromeso.2012.02.012

[22] Qian G, Luo X, Wang J (2008) High bismuth content Bi-MCM-41: synthesis, characterization and investigation on the distribution of bismuth atoms. Microporous Mesoporous Mater 112:632–636. https://doi.org/10.1016/j.micromeso.2007.09.021

[23] Qian G, Lu G, Ji D et al (2005) Oxidation of Cyclohexane over Bi-incorporated MCM-41 mesoporous molecular sieve catalyst with oxygen as oxidant. Chem Lett 34:162–163. https://doi.org/10.1246/cl.2005.162

[24] Sahoo DP, Rath D, Nanda B, Parida KM (2015) Transition metal/metal oxide modified MCM-41 for pollutant degradation and hydrogen energy production: a review. RSC Adv 5:83707–83724. https://doi.org/10.1039/C5RA14555D

[25] Qian G, Ji D, Lu G et al (2005) Bismuth-containing MCM-41: synthesis, characterization, and catalytic behavior in liquid-phase oxidation of cyclohexane. J Catal 232:378–385. https://doi.org/10.1016/j.jcat.2005.03.024

[26] Wang H, Li R, Zheng Y et al (2008) An efficient and reusable catalyst of bismuth-containing SBA-15 mesoporous materials for solvent-free liquid phase oxidation of cyclohexane by oxygen. Catal Lett 122:330–337. https://doi.org/10.1007/s10562-007-9383-3

[27] Yang JH, Cho Y-J, Shin JM, Yim M-S (2015) Bismuth-embedded SBA-15 mesoporous silica for radioactive iodine capture and stable storage. J Nucl Mater 465:556–564. https://doi.org/10.1016/j.jnucmat.2015.06.043

[28] Zhang L, Jaroniec M (2017) SBA-15 templating synthesis of mesoporous bismuth oxide for selective removal of iodide. J Colloid Interface Sci 501:248–255. https://doi.org/10.1016/j.jcis.2017.04.063

[29] Kumar R, Enjamuri N, Pandey JK et al (2015) Bismuth supported SBA-15 catalyst for vapour phase Beckmann rearrangement reaction of cyclohexanone oxime to ε-caprolactam. Appl Catal A Gen 497:51–57. https://doi.org/10.1016/j.apcata.2015.02.044

[30] Xian Q, Chen L, Fan W et al (2022) Facile synthesis of novel Bi0-SBA-15 adsorbents by an improved impregnation reduction method for highly efficient capture of iodine gas. J Hazard Mater 424:127678. https://doi.org/10.1016/j.jhazmat.2021.127678

[31] Kang SW, Yang J-H, Yim M-S (2020) Examining practical application feasibility of Bismuth-embedded SBA-15 for gaseous iodine adsorption. Nucl Technol 206:1593–1606. https://doi.org/10.1080/00295450.2020.1713680

[32] Ward AJ, Weber CC, Masters AF, Maschmeyer T (2013) Application of bismuth-impregnated mesoporous silica to the photochemical oxidation of methylene blue: an example of nanoparticle autocatalysis. ChemCatChem 5:959–965. https://doi.org/10.1002/cctc.201200669

[33] Alshehri AA, Alhanash AM, Eissa M, Hamdy MS (2018) New catalysts with dual-functionality for cyclohexane selective oxidation. Appl Catal A Gen 554:71–79. https://doi.org/10.1016/j.apcata.2018.01.025

[34] Hamdy MS, Al-Shehri BM, Eissa M et al (2021) Low-temperature oxidation of carbon monoxide over Bi-metallic nanoparticles incorporated three dimensional silica. Atmos Environ 244:117955. https://doi.org/10.1016/j.atmosenv.2020.117955

[35] Merlino S, Bonaccorsi E, Armbruster T (1999) Tobermorites; their real structure and order-disorder (OD) character. Am Miner 84:1613–1621. https://doi.org/10.2138/am-1999-1015

[36] Merlino S, Bonaccorsi E, Armbruster T (2001) The real structure of tobermorite 11A: normal and anomalous forms, OD character and polytypic modifications. Eur J Mineral 13:577–590. https://doi.org/10.1127/0935-1221/2001/0013-0577

[37] Zanardi S, Carati A, Cruciani G et al (2006) Synthesis, characterization and crystal structure of new microporous bismuth silicates. Microporous Mesoporous Mater 97:34–41. https://doi.org/10.1016/j.micromeso.2006.07.029

[38] Brunauer S, Emmett PH, Teller E (1938) Adsorption of gases in multimolecular layers. J Am Chem Soc 60:309–319. https://doi.org/10.1021/ja01269a023

[39] Barrett EP, Joyner LG, Halenda PP (1951) The determination of pore volume and area distributions in porous substances. I. Computations from nitrogen isotherms. J Am Chem Soc 73:373–380. https://doi.org/10.1021/ja01145a126

[40] Everett DH, Powl JC (1976) Adsorption in slit-like and cylindrical micropores in the henry's law region. A model for the microporosity of carbons. Journal of the Chemical Society, Faraday Transactions 1: Physical Chemistry in Condensed Phases 72:619. https://doi.org/10.1039/f19767200619

[41] Riesemeier H, Ecker K, Görner W et al (2005) Layout and first XRF applications of the BAM *line* at BESSY II. X-Ray Spectrom 34:160–163. https://doi.org/10.1002/xrs.750

[42] Guilherme Buzanich A, Radtke M, Yusenko KV et al (2023) BAM *line* — a real-life sample materials research beamline. J Chem Phys. https://doi.org/10.1063/5.0157194

[43] Ravel B, Newville M (2020) *ATHENA* and *ARTEMIS*. pp 723–727

[44] Engelhardt G, Koller H (1994) 29Si NMR of Inorganic Solids. pp 1–29

[45] Jaeger C, Hemmann F (2014) Easy: a simple tool for simultaneously removing background, deadtime and acoustic ringing in quantitative NMR spectroscopy—Part I: basic principle and applications. Solid State Nucl Magn Reson 57:22–28. https://doi.org/10.1016/j.ssnmr.2013.11.002

[46] Wei W, Xie J, Meng S et al (2013) Synthetic bismuth silicate nanostructures: photocatalysts grown from silica aerogels precursors. J Mater Res 28:1658–1668. https://doi.org/10.1557/jmr.2013.65

[47] Werner PE, Eriksson L, Westdahl M (1985) TREOR, a semi-exhaustive trial-and-error powder indexing program for all symmetries. J Appl Crystallogr 18:367–370. https://doi.org/10.1107/S0021889885010512

[48] Breck DW (1974) Zeolite molecular sieves: structure, chemistry, and use. Wiley

[49] ZHDANOV SP (1974) Some problems of zeolite crystallization. pp 20–43

[50] Grand J, Awala H, Mintova S (2016) Mechanism of zeolites crystal growth: new findings and open questions. CrystEngComm 18:650–664. https://doi.org/10.1039/C5CE02286J

[51] Mancinelli M, Precisvalle N, Ardit M et al (2023) Thermal stability of templated ZSM-5 zeolites: an in-situ synchrotron X-ray powder diffraction study. Microporous Mesoporous Mater 362:112777. https://doi.org/10.1016/j.micromeso.2023.112777

[52] Wang Y, Wu J, Zhu J et al (2010) The influence of short-chain tetraalkylammonium cations on the recrystallization of magadiite into zeolites. Microporous Mesoporous Mater 135:143–148. https://doi.org/10.1016/j.micromeso.2010.07.002

[53] Shah KKr, Saikia J, Saikia D, Talukdar AK (2012) Synthesis and characterization of isomorphously zirconium substituted Mobil Five (MFI) zeolite. Mater Chem Phys 134:43–49. https://doi.org/10.1016/j.matchemphys.2012.02.012

[54] Zhang Q, Gao S, Yu J (2023) Metal sites in zeolites: synthesis, characterization, and catalysis. Chem Rev 123:6039–6106. https://doi.org/10.1021/acs.chemrev.2c00315

[55] Paul G, Bisio C, Braschi I et al (2018) Combined solid-state NMR, FT-IR and computational studies on layered and porous materials. Chem Soc Rev 47:5684–5739. https://doi.org/10.1039/C7CS00358G

[56] Wang Y, Zhao J, Zhao X et al (2009) A facile water-based process for preparation of stabilized Bi nanoparticles. Mater Res Bull 44:220–223. https://doi.org/10.1016/j.materresbull.2008.03.026

[57] Ouis MA, El Batal FH, Azooz MA (2020) FTIR, optical, and thermal studies of cadmium borate glass doped with Bi2O3 and effects of gamma irradiation. J Aust Ceram Soc 56:283–290. https://doi.org/10.1007/s41779-019-00429-0

[58] Wang L, Zhang Z, Yin C et al (2010) Hierarchical mesoporous zeolites with controllable mesoporosity

templated from cationic polymers. Microporous Mesoporous Mater 131:58–67. https://doi.org/10.1016/j.micromeso.2009.12.001

[59] Moliner M, González J, Portilla MT et al (2011) A new aluminosilicate molecular sieve with a system of pores between those of ZSM-5 and beta zeolite. J Am Chem Soc 133:9497–9505. https://doi.org/10.1021/ja2015394

[60] Carroll SA, Maxwell RS, Bourcier W et al (2002) Evaluation of silica-water surface chemistry using NMR spectroscopy. Geochim Cosmochim Acta 66:913–926. https://doi.org/10.1016/S0016-7037(01)00827-4